Intensity- and Temperature-Dependent Carrier Recombination in $\mathrm{InAs/InAs_{1-x}Sb_x}$ Type-II Superlattices

B. V. Olson,[*] E. A. Kadlec, J. K. Kim, J. F. Klem, S. D. Hawkins, and E. A. Shaner
Sandia National Laboratories, Albuquerque, New Mexico 87185, USA

M. E. Flatté
Department of Physics and Astronomy and Optical Science and Technology Center,
The University of Iowa, Iowa City, Iowa 52242, USA

(Received 8 December 2014; revised manuscript received 21 January 2015; published 17 April 2015)

Time-resolved measurements of carrier recombination are reported for a midwave infrared $\mathrm{InAs/InAs_{0.66}Sb_{0.34}}$ type-II superlattice (T2SL) as a function of pump intensity and sample temperature. By including the T2SL doping level in the analysis, the Shockley-Read-Hall (SRH), radiative, and Auger recombination components of the carrier lifetime are uniquely distinguished at each temperature. SRH is the limiting recombination mechanism for excess carrier densities less than the doping level (the low-injection regime) and temperatures less than 175 K. A SRH defect energy of 95 meV, either below the T2SL conduction-band edge or above the T2SL valence-band edge, is identified. Auger recombination limits the carrier lifetimes for excess carrier densities greater than the doping level (the high-injection regime) for all temperatures tested. Additionally, at temperatures greater than 225 K, Auger recombination also limits the low-injection carrier lifetime due to the onset of the intrinsic temperature range and large intrinsic carrier densities. Radiative recombination is found to not have a significant contribution to the total lifetime for all temperatures and injection regimes, with the data implying a photon recycling factor of 15. Using the measured lifetime data, diffusion currents are calculated and compared to calculated $\mathrm{Hg_{1-x}Cd_xTe}$ dark current, indicating that the T2SL can have a lower dark current with mitigation of the SRH defect states. These results illustrate the potential for $\mathrm{InAs/InAs_{1-x}Sb_x}$ T2SLs as absorbers in infrared photodetectors.

DOI: 10.1103/PhysRevApplied.3.044010

I. INTRODUCTION

The minority-carrier lifetime (τ_{MC}) is a critical parameter for infrared (IR) photodetectors, as it determines both the dark current and maximum operating temperature. For a diffusion-limited photodetector, the dark current is inversely proportional to τ_{MC} as

$$J_{\mathrm{diff}} = q\frac{n_i^2 W}{n_0 \tau_{\mathrm{MC}}}, \tag{1}$$

where q is the electron charge, n_i is the intrinsic carrier density, n_0 is the majority-carrier electron density, and W is the absorber thickness [1,2]. Note, this equation applies when the minority-carrier diffusion length is greater than the absorber thickness. This equation implies that long carrier lifetimes are ideal and will minimize the detector dark current. $\mathrm{InAs/InAs_{1-x}Sb_x}$ type-II superlattices (T2SLs) have recently gained interest for next-generation IR sensors due to their realization of long microsecond-scale τ_{MC} [3–5]. These reported lifetimes are significantly longer than those measured in the more commonly used $\mathrm{InAs/In_xGa_{1-x}Sb}$ T2SL system [6–10] and are, instead, similar in magnitude to those reported for $\mathrm{Hg_{1-x}Cd_xTe}$ (MCT), the current state-of-the-art IR photodetector material [6,11]. The long lifetimes suggest that a lower dark current can be attained in the $\mathrm{InAs/InAs_{1-x}Sb_x}$ T2SL compared to $\mathrm{InAs/In_xGa_{1-x}Sb}$ T2SLs for similarly doped material and that $\mathrm{InAs/InAs_{1-x}Sb_x}$ T2SLs may compete with MCT. For both of these T2SL material systems, high-performance photodetectors have been demonstrated [12–15], yet the level of device performance predicted by theory has not yet been reported [16–18]. For the case of $\mathrm{InAs/In_xGa_{1-x}Sb}$ T2SLs, the large dark currents are primarily a result of the aforementioned short τ_{MC}, which is limited by carrier recombination at Shockley-Read-Hall (SRH) defects. It has recently been shown that defects related to $\mathrm{In_xGa_{1-x}Sb}$ are likely the cause of these persistent mid-band-gap SRH generation-recombination centers [19,20]. As there are significantly fewer reports for the $\mathrm{InAs/InAs_{1-x}Sb_x}$ T2SL material system, it is necessary to understand more clearly the recombination mechanisms that are limiting τ_{MC}. Through Eq. (1), which offers a concrete link between photodetector performance and the intangible internal charge-carrier dynamics, greater insight into the limitations of $\mathrm{InAs/InAs_{1-x}Sb_x}$ T2SL photodetectors can then be made. This insight will, in turn, lead to strategies to improve device performance.

The primary mechanisms contributing to the dark current in an IR photodetector, for modest reverse biases and

---

[*] benolso@sandia.gov

typical temperatures, is carrier generation in both the undepleted and depleted portions of the T2SL absorber. Both carrier generation in the undepleted (diffusion current) and the depleted (generation-recombination current) regions are dependent on the carrier lifetime [2,21] and, therefore, understanding the nonequilibrium carrier-recombination dynamics is important. Previous studies have shown that temperature-dependent optical measurements are a powerful tool to, for example, elucidate various recombination mechanisms [5,20,22], characterize sub-band-gap optical generation rates [23], or investigate potential materials for IR emitter applications [24] in narrow-band-gap type-II systems. In this paper, we outline an approach for separating the contributions of the various recombination mechanisms as a function of excitation intensity at a single temperature and apply it to quantify recombination lifetimes associated with these mechanisms in a high-quality midwavelength IR (MWIR) InAs/$\mathrm{InAs}_{1-x}\mathrm{Sb}_x$ T2SL. Carrier lifetimes are reported both as a function of sample temperature and pump intensity (i.e., the excess carrier density, Δn). By taking into account the dependence that SRH, radiative, and Auger recombination have with the T2SL doping level, their contributions to the measured total lifetimes are uniquely determined. Currently, there are no reports of defect characterization in InAs/$\mathrm{InAs}_{1-x}\mathrm{Sb}_x$ T2SLs using such direct methods as deep-level transient spectroscopy [25] or admittance spectroscopy [26], leaving carrier-lifetime analysis as the primary method of determining defect energy levels in this material system.

II. SAMPLE AND METHODS

The sample is grown using molecular beam epitaxy on a 3-in. tellurium-doped GaSb substrate with a (100) orientation. The superlattice growth layer consists of an approximate 4-μm-thick unintentionally doped 4.2-nm InAs/1.55-nm $\mathrm{InAs}_{0.66}\mathrm{Sb}_{0.34}$ T2SL absorber layer integrated into a photodetector architecture. The T2SL band-gap energy (E_g) is approximately 232 meV (5.35 μm) at 100 K. Carrier lifetimes are measured from an unprocessed portion of the sample wafer using a time-resolved microwave reflectance (TMR) method. This apparatus includes a tunable optical parametric oscillator producing optical pulses with approximately 10-ns full-width-at-half-maximum pulse width at a repetition rate of 1 kHz, used to excite the sample under study. These pump pulses are tuned near the band-gap energy of the T2SL absorbing layer; in this case, a wavelength of 3.7 μm is used to ensure excess carriers are generated as uniformly as possible throughout the thick T2SL. At this wavelength, the absorption coefficient in the T2SL is approximately 3600 cm^{-1} [22]. The pump beam is focused to a radius (e^{-1} of the intensity) of 2700 μm onto the substrate side of the sample under study, which is housed in a low-vibration cryostat for temperature control. The loss of the pump in the substrate is estimated using an absorption coefficient of 10 cm^{-1}, which is a typical value for the manufacturer's quoted electron density at this wavelength [27]. The incident pump fluence is varied using ZnSe polarizers as attenuators.

At zero time, a pump pulse optically generates a hot distribution of electron-hole pairs throughout the T2SL absorber, perturbing the sample into a nonequilibrium state. On a time scale that is fast compared to carrier recombination, these excited charge carriers cool to the T2SL band edges and alter the conductivity of the absorber. Microwave radiation reflected by the front side of the sample is then used to probe this change in conductivity and, hence, the excited carrier density [28]. The decay of these excess carriers back to equilibrium is temporally resolved by monitoring the reflected microwave signal as a function of time. For this TMR system, a 95-GHz microwave Gunn diode provides the source of the microwaves and any reflected microwaves are sent to a microwave detector via a circulator. The transient TMR decays are then amplified using a wide-bandwidth preamplifier and averaged using a high-resolution digital oscilloscope.

The equilibrium electron densities (n_0) of the n-type T2SL absorber determined using capacitance-voltage (CV) measurements on portions of the sample wafer that are fabricated into test photodetector pixels are shown in Fig. 1. At 100 K, n_0 is approximately 8×10^{14} cm^{-3}. The temperature dependence of n_0, the equilibrium minority hole density (p_0), and n_i are also shown in Fig. 1, calculated using 14-band $\mathbf{k} \cdot \mathbf{p}$ software [29] for the unintentional doping level determined from the CV measurements. In the extrinsic temperature range corresponding to temperatures < 175 K, n_0 is independent from the temperature. As the temperature increases beyond 175 K, n_i begins to dominate, and due to the law of mass action (i.e., $n_0 p_0 = n_i^2$), the equilibrium electron density must also increase. This

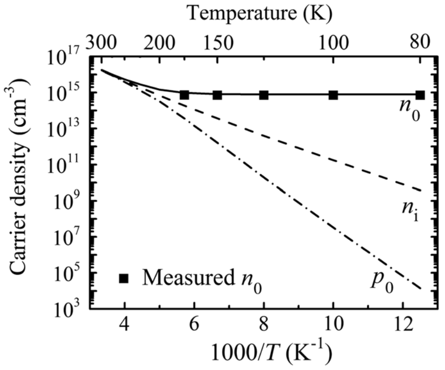

FIG. 1. Experimentally determined equilibrium electron densities, or n_0 values, from capacitance-voltage measurements on test photodetector pixels fabricated from the sample wafer (symbols). The curves correspond to equilibrium carrier densities calculated using $\mathbf{k} \cdot \mathbf{p}$ software for the 4.2-nm InAs/1.55-nm $\mathrm{InAs}_{0.66}\mathrm{Sb}_{0.34}$ T2SL structure and a doping level of 8×10^{14} cm^{-3}.

transition from the extrinsic to intrinsic temperature regimes occurs between 175 and 225 K. There are also two important regimes when comparing the nonequilibrium excess carrier density (Δn) to n_0. The first, which is also the most important for IR photodetectors, is when $\Delta n \ll n_0$. This regime is referred to as the low-injection regime, and it is where minority-carrier recombination occurs. In this low-injection regime, the carrier lifetime is equal to τ_{MC} and is either independent from or, in some cases, weakly dependent on Δn. The second is the high-injection regime, where $\Delta n \gg n_0$. In this regime, the carrier lifetime has a significant dependence on Δn.

III. EXPERIMENT RESULTS

Time-resolved decays of carrier recombination in the T2SL absorber are shown in Fig. 2 for multiple sample temperatures and pump intensities corresponding to different initial optically generated excess carrier densities. For brevity, a representative subset of temperatures and injected carrier densities is shown. During the first couple hundreds of nanoseconds following the generation of excess carriers, a fast initial decay is observed in the TMR data and can be seen in the inset to the 100-K data in Fig. 2. This rapid initial decay becomes less pronounced as the incident pump fluence and, therefore, Δn, is decreased, which indicates that Auger and/or radiative recombination are the dominant recombination mechanisms during this time period. On a microsecond time scale, the decays lengthen and approach a mono-exponential decay, indicating that Δn is reduced by carrier recombination and is now similar to or less than n_0. For temperatures below 200 K, a slight bowing of the long decays is noticeable (i.e., a slow decay followed by a slightly faster decay). This bowing can be seen in Fig. 2 for the 100- and 150-K data, where the long-time-scale decays display two distinguishable and unique time constants. The arrows highlight the inflection point between these two different decay times. This type of carrier decay suggests saturation of SRH recombination centers [30], which is characterized by a SRH-limited τ_{MC} with a majority-carrier SRH lifetime (τ_{n_0}) that is longer than the minority-carrier SRH lifetime (τ_{p_0}). This effect has been previously observed in InAs/In$_x$Ga$_{1-x}$Sb T2SLs, although the effect is less dramatic here [20,31]. For temperatures greater than 200 K, this feature is not present, and the decays are single exponential after the initial rapid decays, suggesting a mechanism besides SRH recombination limits the carrier lifetimes at these temperatures.

To investigate carrier recombination in more detail, the TMR decay data in Fig. 2 are transformed into instantaneous carrier lifetimes as a function of Δn using

$$\tau^{-1} = -\frac{1}{\Delta n}\frac{\partial \Delta n}{\partial t} = -\frac{1}{\Delta n}\frac{\partial \Delta n}{\partial S}\frac{\partial S}{\partial t}, \tag{2}$$

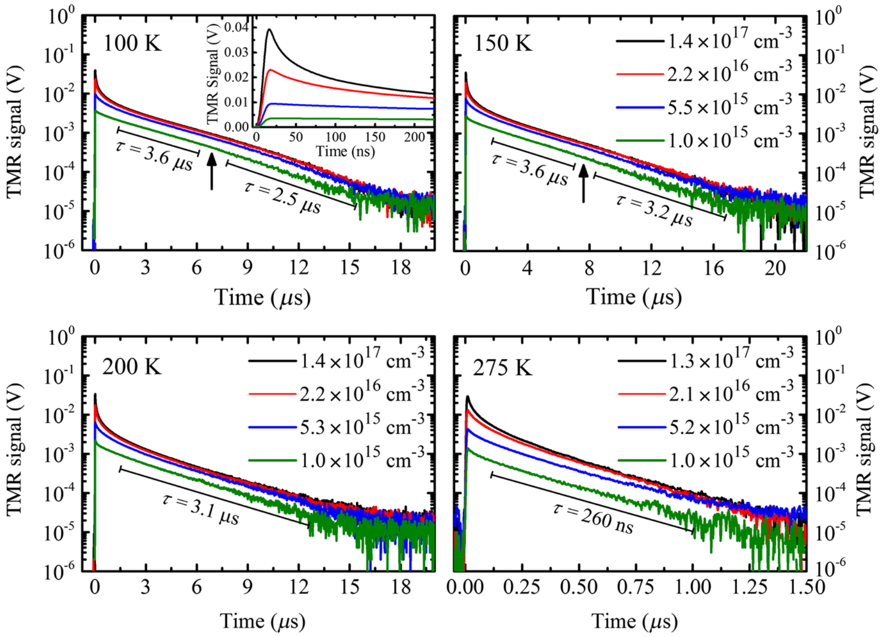

FIG. 2. Time-resolved microwave reflectance decays of carrier recombination in the MWIR InAs/InAs$_{0.66}$Sb$_{0.34}$ T2SL absorber. Data are shown for multiple different initial optically generated carrier densities and sample temperatures. The 100-K decays correspond to the same initial carrier densities as the 150-K data. The arrows in the top two plots highlight the subtle bowing of the long-time-scale component of the decay curves. Decay time constants are also shown for different sections of these long-time-scale decays. The inset to the 100-K plot shows the fast initial decays which occur during the first few hundred nanoseconds at large excess carrier densities.

where S is the TMR signal. The term $\partial\Delta n/\partial S$ is determined using the dependence that the maximum TMR signal observed shortly after zero time delay has on the optically injected carrier density [3,32]. $\partial S/\partial t$ is determined using the time-resolved decays in Fig. 2. The resulting carrier-recombination rate data are then inverted such that the final results are carrier lifetimes as a function of Δn shown in Fig. 3. The carrier lifetimes are highly dependent on Δn for carrier densities that are greater than approximately 2×10^{15} cm^{-3} corresponding to the high-injection regime. For Δn less than approximately 1×10^{15} cm^{-3}, the lifetimes are very weakly dependent on Δn at low temperatures and constant at high temperatures. For all temperatures, the lifetime becomes independent from Δn for very small densities approaching 10^{13} cm^{-3}, indicating that the low-injection regime has been reached. Very good fidelity is observed in the low-injection regime, which is necessary to accurately measure τ_{MC} and highlights the utility of the TMR method for characterizing carrier lifetimes in these small-band-gap materials. The transition between these two regimes corresponding to $\Delta n \approx (0.7-2)\times 10^{15}$ cm^{-3} at low temperature is consistent with the measured doping level of the T2SL absorber and confirms that the calibration of the initial injected carrier densities and transformation of the TMR decays is without significant error.

IV. CARRIER-LIFETIME THEORY

For a bulk semiconductor, the total carrier lifetime (τ) can be written as a combination of the SRH lifetime (τ_{SRH}), the radiative lifetime (τ_{rad}), and the Auger lifetime (τ_{Auger}) as

$$\tau^{-1} = \tau_{\mathrm{SRH}}^{-1} + \tau_{\mathrm{rad}}^{-1} + \tau_{\mathrm{Auger}}^{-1}. \tag{3}$$

In practice, it can be difficult to determine which of these mechanisms limit the carrier lifetime. Fortunately, these mechanisms each have unique dependencies on Δn, n_0, and temperature, which are exploited here to determine their individual contributions to the total carrier lifetime. The following discussion pertains to n-type material and $n_0 \gg p_0$ is routinely assumed. This analysis is easily extendable to p-type semiconductors with the proper substitutions. It is also assumed that the excess electron density equals the excess hole density, and both quantities are referred to simply as the excess carrier density, Δn. This assumption is valid for optical generation of charge carriers.

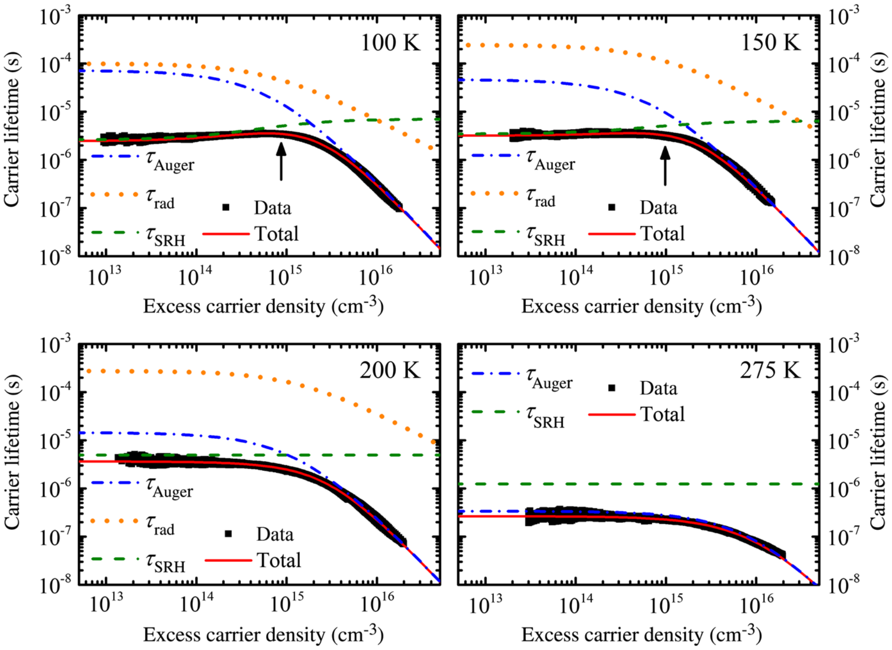

FIG. 3. Carrier lifetimes as a function of excess carrier density and temperature (symbols) determined from the intensity-dependent time-resolved microwave measurements. The solid red curves are best fits to the measured data and represent the total carrier lifetime τ. The dashed, dotted, and dash-dotted curves are the deconvolved contributions of SRH, radiative, and Auger recombination to the total lifetime, respectively, where $\tau = (\tau_{\mathrm{SRH}}^{-1} + \tau_{\mathrm{rad}}^{-1} + \tau_{\mathrm{Auger}}^{-1})^{-1}$ and are found from the extracted fit parameters of the total lifetime fit. For temperatures greater than 200 K the measured lifetimes are almost entirely described by SRH and Auger recombination. The radiative lifetimes at these temperatures could therefore not be reliably determined and are not shown. The arrows in the top two plots highlight the effect of SRH trap saturation, where the carrier lifetime is observed to reach a maximum at excess carrier densities near the doping level and then trend towards a shorter lifetime for $\Delta n \ll n_0$.

The SRH lifetime for a single defect level is given by [33]

$$\tau_{\mathrm{SRH}}^{-1} = \frac{1}{\Delta n}\frac{np - n_0 p_0}{\tau_{p_0}(n+n_1) + \tau_{n_0}(p+p_1)} = \frac{n_0 + p_0 + \Delta n}{\tau_{p_0}(n+n_1) + \tau_{n_0}(p+p_1)}, \quad (4)$$

with

$$n_1 = n_i e^{(E_t - E_i)/k_B T}, \qquad p_1 = n_i e^{(E_i - E_t)/k_B T}, \quad (5)$$

or if the material is approximated as three dimensional, then

$$n_1 = N_c e^{(E_t - E_c)/k_B T}, \qquad p_1 = N_v e^{(E_v - E_t)/k_B T}, \quad (6)$$

where $n = n_0 + \Delta n$, $p = p_0 + \Delta n$, E_i and E_t are the intrinsic Fermi and SRH defect energies, E_c and E_v are the T2SL conduction- and valence-band energies, N_c and N_v are the effective conduction- and valence-band density of states, respectively, k_B is Boltzmann's constant, and T is the temperature. The SRH lifetime is governed by the two before-mentioned characteristic lifetimes,

$$\tau_{n_0} = (\sigma_n v_n N_t)^{-1}, \qquad \tau_{p_0} = (\sigma_p v_p N_t)^{-1}, \quad (7)$$

where σ_n and σ_p are the electron and hole defect capture cross sections, v_n and v_p are the electron and hole thermal velocities, respectively, and N_t is the defect density. Assuming n-type material and a defect level near mid-band-gap, Eq. (4) becomes [30]

$$\tau_{\mathrm{SRH}}^{-1} = \frac{n_0 + \Delta n}{\tau_{p_0}(n_0 + \Delta n) + \tau_{n_0}\Delta n}, \quad (8)$$

which describes the density dependence of SRH recombination. The density-independent character of SRH recombination ($\tau_{\mathrm{SRH}} = \tau_{p_0}$ for n-type material) can be arrived at by assuming either $\tau_{n_0} \ll \tau_{p_0}$ or $\Delta n \ll n_0$.

The radiative lifetime in thick absorbing material is [33]

$$\tau_{\mathrm{rad}}^{-1} = B\frac{(np - n_0 p_0)}{\Delta n} = B(n_0 + p_0 + \Delta n), \quad (9)$$

where B is the bulk radiative coefficient. For n-type material,

$$\tau_{\mathrm{rad}}^{-1} = B(n_0 + \Delta n). \quad (10)$$

This equation defines the bulk radiative lifetime and is related to the microscopic radiative lifetime (τ_{MR}) through

$$\tau_{\mathrm{rad}} = \phi \tau_{\mathrm{MR}}, \quad (11)$$

where ϕ is the photon recycling factor. The microscopic radiative lifetime is similarly written as

$$\tau_{\mathrm{MR}}^{-1} = B_r(n_0 + \Delta n), \quad (12)$$

where B_r is the microscopic radiative coefficient defined by van Roosbroeck and Shockley (VRS) [34]. The relationship between the measured bulk and microscopic coefficients is, thus,

$$B = B_r/\phi. \quad (13)$$

Photon recycling acts to increase τ_{rad} through the reabsorption of emitted photons and is greater for material with greater absorptivity and/or thicker absorbing layers. Note, as the sample thickness decreases $\phi \to 1$ and B and τ_{rad} converge to B_r and τ_{MR}, respectively.

The Auger lifetime can be written as [35]

$$\tau_{\mathrm{Auger}}^{-1} = \frac{C_n(np - n_0 p_0)n + C_p(np - n_0 p_0)p}{\Delta n} = C_n(n_0 + p_0 + \Delta n)n + C_p(n_0 + p_0 + \Delta n)p, \quad (14)$$

where C_n and C_p are the Auger coefficients corresponding to the Auger-1 and Auger-7 processes, respectively, and are in units of cm^6/s. Auger-1 recombination occurs when an electron recombines with a hole and the excess energy is imparted to a second electron, which is excited to a higher-lying conduction-band state. The Auger-7 process is similar, except the excess energy is imparted to a hole which is excited to a higher-energy valence-band state in the light-hole band. The initial and final states in Auger transitions are not required to be at zone center and significant kinetic energy can be involved, with the constraint that both energy and momentum are conserved. While there are more possible Auger transitions involving different initial and final states, the Auger-1 and Auger-7 transitions have the lowest threshold energy and are the only ones of practical concern [36]. Additionally, since the Auger-1 process involves two electrons, it will be the dominant Auger recombination mechanism in n-type material. The Auger-7 process will be the dominate Auger recombination mechanism in p-type material due to this process involving primarily holes. For high-injection levels, $\tau_{\mathrm{Auger}}^{-1}$ has the limiting form,

$$\tau_{\mathrm{Auger}}^{-1} \approx (C_n + C_p)\Delta n^2. \quad (15)$$

Because of the quadratic scaling with Δn, which is of higher order than both radiative or SRH recombination, Auger recombination will eventually dominate at large-enough injection levels [4,37–39]. Auger coefficients measured under high-injection levels are also inherently equal to the sum of the electron- and hole-dominated Auger processes. If n-type material and low-injection levels are imposed, Eq. (14) has the limiting form,

$$\tau_{\mathrm{Auger}}^{-1} \approx C_n n_0^2, \quad (16)$$

which is the Auger recombination contribution to τ_{MC} and is seen to depend on C_n and not C_p. The Auger coefficients reported here are determined from the high-injection lifetimes, and, therefore, one must have knowledge of C_p in order to use these measured coefficients to determine the low-injection Auger contribution to τ_{MC}. The authors note that n-type and p-type Auger processes have been experimentally distinguished by measuring τ_{MC} as a function of dopant type and level, but required multiple samples [40]. Unfortunately, little information exists on Auger lifetimes in $\mathrm{InAs/InAs}_{1-x}\mathrm{Sb}_x$ T2SLs. While Auger lifetimes have been extensively investigated in the $\mathrm{InAs/In}_x\mathrm{Ga}_{1-x}\mathrm{Sb}$ T2SL material system [17,38,39,41], we find no theoretical calculations or experimental evidence comparing n-type to p-type Auger processes in the $\mathrm{InAs/InAs}_{1-x}\mathrm{Sb}_x$ T2SL system investigated here. Auger processes in T2SLs are highly dependent on the nonparabolic and anisotropic superlattice band structure, both of which are tied to the degree of quantum confinement from the type-II band offset and layer strains [17]. Drawing inferences from other type-II material systems with different constituent-layer band-gap energies, such as $\mathrm{InAs/In}_x\mathrm{Ga}_{1-x}\mathrm{Sb}$, can, therefore, be difficult, and a more rigorous investigation of n-type and p-type Auger recombination processes in $\mathrm{InAs/InAs}_{1-x}\mathrm{Sb}_x$ T2SLs is necessary.

Since the Auger-1 and Auger-7 processes are fundamentally similar, a dimensionless factor (γ) is often used to relate the Auger-1 recombination rate (R_{A1}) to the Auger-7 recombination rate (R_{A7}) [42],

$$R_{A7} = \frac{R_{A1}}{\gamma}\frac{p}{n}. \tag{17}$$

In terms of the Auger coefficients, this relationship is

$$C_p = C_n/\gamma. \tag{18}$$

Because of the lack of available information, it is assumed here that $\gamma \to \infty$, and the hole-dominated Auger-7 process is neglected in the analysis. By doing so, the Auger coefficient measured at high-injection levels is assumed to be entirely due to the Auger-1 process, and the maximum Auger recombination contribution to τ_{MC} is used. Using this assumption, Eq. (14) can be written as

$$\tau_{\mathrm{Auger}}^{-1} = C_n(n_0 + \Delta n)^2. \tag{19}$$

Using Eqs. (3), (8), (10), and (19), the total lifetime is, thus,

$$\tau^{-1} = \frac{n_0 + \Delta n}{\tau_{p_0}(n_0 + \Delta n) + \tau_{n_0}\Delta n} + B(n_0 + \Delta n) + C_n(n_0 + \Delta n)^2, \tag{20}$$

with τ_{MC} determined from the low-injection limit as

$$\tau_{\mathrm{MC}}^{-1} = \lim_{\Delta n \to 0} \tau^{-1} = \tau_{p_0}^{-1} + Bn_0 + C_n n_0^2. \tag{21}$$

The solid red curves in Fig. 3 are best fits to the measured lifetime data using Eq. (20). For the fitting procedure, n_0 is fixed using the data in Fig. 1 for that particular sample temperature, and τ_{p_0}, τ_{n_0}, B, and C_n are allowed to vary for the best fit to the measured data. Since each recombination mechanism has a unique dependence on Δn and n_0, and the data cover both injection regimes with high fidelity, the individual contributions of each to the total lifetime are uniquely distinguished from one another at each temperature. These lifetime components are also shown in Fig. 3. Because of the significant contributions of Auger and SRH recombination, the radiative lifetime at temperatures greater than 200 K cannot be reliably determined and are not shown. From the results presented in Fig. 3, τ_{MC} is found using Eq. (21) and the coefficients from the fitting results. The temperature dependence of the measured τ_{MC} values is shown in Fig. 4, where the low-injection SRH, radiative, and Auger components of τ_{MC} are also plotted.

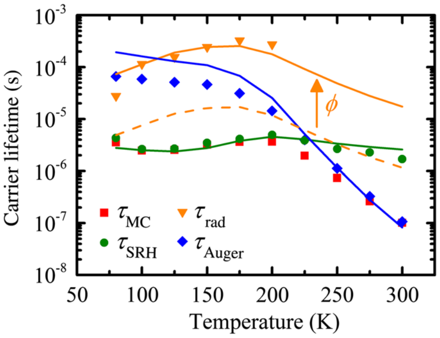

FIG. 4. Measured minority-carrier lifetimes (red squares) and low-injection-level SRH, radiative, and Auger lifetime components that make up the minority-carrier lifetime (green circles, orange triangles, and blue diamonds, respectively). The solid green curve is a best fit to the SRH lifetime component to extract the SRH defect energy and properties. The dashed orange curve is the microscopic radiative lifetime calculated from the T2SL band structure using $\mathbf{k}\cdot\mathbf{p}$ software. The solid orange curve is the calculated radiative lifetime scaled using a photon recycling factor, ϕ, of 15. The solid blue curve is the calculated Beattie, Landsberg, and Blakemore Auger-1 lifetime using $|F_1F_2| = 0.11$ and $m_e/m_h = 0.114$.

V. DISCUSSION

A. Shockley-Read-Hall recombination

From Fig. 4, SRH recombination is observed to limit τ_{MC} at temperatures below 175 K in the low-injection regime. A similar result was reported earlier by us using time-resolved pump-probe measurements [22], corresponding to the temperature range where SRH trap saturation is apparent in the TMR decays (see Fig. 2). Under the condition that $\tau_{n_0} \ll \tau_{p_0}$, electrons are captured quickly by SRH defect centers, SRH recombination is governed by the capture time of holes, and the SRH lifetime is independent from Δn in both injection regimes, which is not the case observed here. If τ_{n_0} is, however, similar in magnitude or greater than τ_{p_0} and for excess carrier densities similar to n_0, the SRH centers can become saturated with holes and the lifetime, instead, is determined by the slower capture of electrons, resulting in a longer lifetime. Once the low-injection regime is reached though, SRH recombination returns to being governed by the shorter τ_{p_0} and the lifetime is shorter. This saturation of the SRH recombination centers is the effect that causes the measured carrier lifetimes to reach a maximum at $\Delta n \approx n_0$ and then trend towards a slightly shorter lifetime when $\Delta n \ll n_0$ in the 80- to 175-K temperature range (see Fig. 3). In the temperature range of 175 to 225 K, SRH is still the primary recombination mechanism; however, trap saturation is less apparent at these temperatures. Ultimately, for temperatures nearing ambient, this effect is not observed at all in the data, and the carrier lifetimes are a constant for $\Delta n < n_0$. As SRH trap saturation can be observed only when τ_{MC} is limited by SRH recombination; the loss of this behavior at higher temperatures is an effect of entering the intrinsic temperature regime and Auger recombination becoming the dominant mechanism controlling the lifetime.

The SRH defect energy level and properties are determined from the low-injection-level SRH component of τ_{MC}. Per Eqs. (5) and (6), the temperature dependence of either the T2SL band-gap energy or intrinsic Fermi energy are therefore required. Figure 5(a) shows measured time-integrated photoluminescence (PL) spectra of the T2SL absorber for temperatures between 80 and 300 K. From these data, the peak PL energy is determined and is shown in Fig. 5(b). Also shown in Fig. 5(b) are $\mathbf{k}\cdot\mathbf{p}$ calculated results of the temperature dependence of the T2SL band-gap energy and intrinsic Fermi energy. It has been reported that peak PL energies can be greater than the band-gap energy by 2–3k_BT due to thermal effects [43]. With this effect in mind, there is very good agreement between the peak PL energies and the independently calculated T2SL band-gap energies when $2k_BT$ is subtracted from the measured data. These data, along with Eqs. (4)–(7), are then used to fit the low-injection SRH lifetime component of τ_{MC}. It is assumed for this fit that $\sigma_n = \sigma_p = \sigma$ and the resulting best fit found for $E_t =$ 95 meV and $\sigma N_t = 0.03\ \mathrm{cm}^{-1}$. These values are similar to those reported previously where n_0 was assumed temperature independent in the analysis of τ_{MC} [22]. Because of the ambiguity of the governing SRH lifetime equations for a mid-band-gap defect level, similar fits are achieved for a defect level either 95 meV above the T2SL valence-band edge or below the T2SL conduction-band edge.

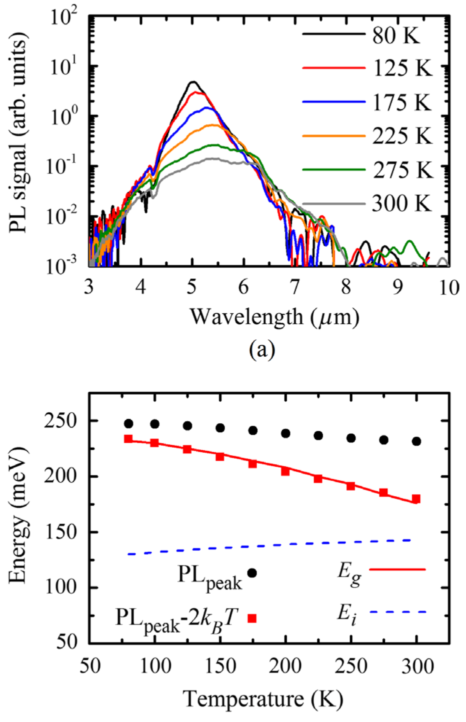

(a)

(b)

FIG. 5. (a) Measured time-integrated photoluminescence spectra of the T2SL absorber as a function of temperature. The modulation at 4.25 μm is due to $\mathrm{CO_2}$ absorption. (b) Peak PL energy as a function of temperature (black circles) and corresponding energy when $2k_BT$ is subtracted to account for thermal shifts (red squares). The curves in (b) are independently calculated T2SL band-gap (E_g) and intrinsic Fermi (E_i) energies.

It was recently proposed by Grein *et al.* [44] that the effectiveness of defects in T2SLs can potentially be mitigated by engineering the superlattice structure to shift the absolute band-gap energy away from the defect state. In this manner, a midgap SRH defect level can potentially be shifted closer to a band edge, where the benefit is that shallow defect levels are less effective as SRH centers than deep defect levels. This mitigation strategy has implications for device applications, as a lower dark current can be attained by proper engineering of the T2SL absorber structure instead of increasing the material quality. For $\mathrm{InAs/InAs_{1-x}Sb_x}$ T2SLs, this strategy requires adjusting the layer thicknesses and $\mathrm{InAs_{1-x}Sb_x}$ composition to retain strain balancing and the same band gap but shift the absolute energy position of the band gap. Designs of this nature have been reported for MWIR $\mathrm{InAs/InAs_{1-x}Sb_x}$ T2SLs, where some effect on τ_{MC} was observed [32]. However, it has yet to be reported if these structures indeed shifted the T2SL band gap relative to the defect state. To account for the 95-meV defect energy identified here, this shift in absolute energy needs to be significant. It is also noted that the most direct methods of characterizing defect states are methods like deep-level transient spectroscopy and admittance spectroscopy. Until these methods are successfully demonstrated for narrow-band-gap T2SLs though, carrier-lifetime analysis, such as is presented here, remains the most effective way of determining SRH trap energies and if this proposed defect mitigation strategy works.

B. Auger recombination

The results presented in Fig. 3 show that Auger recombination is the limiting mechanism for all temperatures in the high-injection regime. Auger recombination is also shown to be the limiting mechanism in the low-injection regime for temperatures greater than 225 K, corresponding

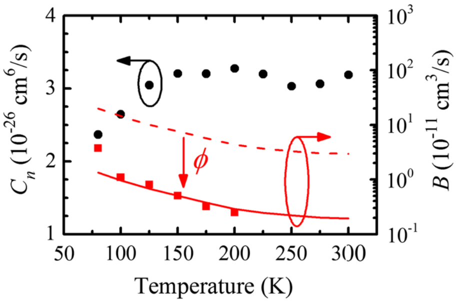

FIG. 6. Experimental Auger (black circles) and radiative (red squares) coefficients as a function of temperature determined from the carrier-lifetime fitting results. The dashed red curve is $\mathbf{k}\cdot\mathbf{p}$ calculated B_r coefficients. The solid red curve is the same calculated microscopic radiative coefficients scaled using a photon recycling factor of 15.

to the intrinsic temperature range and large intrinsic carrier densities. This result is not surprising, as this T2SL material system exhibits relatively large Auger recombination rates, and since Auger recombination scales quadratically with the carrier density, it dominates SRH and radiative recombination at either large Δn or n_i. The measured C_n coefficients are plotted as a function of temperature in Fig. 6. The uncertainty in the C_n coefficients is estimated to be a factor of 2 to 3. Because of the quadratic dependence of τ_{Auger}^{-1} on Δn, Auger coefficients are most sensitive to the calibration of the initial injected carrier densities. While great care is taken to accurately calibrate these carrier densities, measurement errors in the pump spot radius, pump pulse energies, losses due to cryostat windows and the sample substrate, as well as Fresnel reflections from the sample surface, do occur and are taken into account when arriving at the uncertainty. The coefficients reported here are consistent, within our estimated uncertainty, with Auger coefficients reported previously using different experimental techniques and test geometries for this T2SL material system [3,32]. Interestingly, for $T > 150$ K, C_n becomes independent from the temperature. These values are also significantly larger than those reported for InAs/In$_x$Ga$_{1-x}$Sb T2SLs [3,7,45], which has potential impact for optical emitter designs utilizing InAs/InAs$_{1-x}$Sb$_x$ T2SLs.

The temperature dependence of the Auger-1 lifetime can be determined using the analytical expressions by Beattie, Landsberg [46], and Blakemore [35] (BLB) defined as

$$\tau_{\text{Auger}}^{\text{BLB}} = \frac{2n_i^2}{n_0^2 + n_0 p_0}\tau_{A1}^{(i)}, \tag{22}$$

where the intrinsic Auger-1 lifetime $\tau_{A1}^{(i)}$ is

$$\tau_{A1}^{(i)} = 3.8 \times 10^{-18}\frac{\epsilon_\infty^2 (1+\mu)^{1/2}(1+2\mu)}{(m_e/m_o)|F_1F_2|^2} \times \left(\frac{E_g}{k_B T}\right)^{3/2} \exp\left(\frac{1+2\mu}{1+\mu}\frac{E_g}{k_B T}\right), \tag{23}$$

where ϵ_∞ is the high-frequency dielectric constant, $\mu = m_e/m_h$, m_e is the electron effective mass, m_h is the hole effective mass, m_o is the free-electron mass, and $|F_1F_2|$ is a temperature-independent Bloch function overlap parameter. The BLB lifetime shown in Fig. 4 compared to the extracted Auger lifetimes is calculated using $\epsilon_\infty = 13.5$ determined using an interpolation of bulk InAs and InSb values [47], density-of-states masses of $m_e = 0.029m_o$ and $m_h = 0.2544m_o$ [5], and $|F_1F_2| = 0.11$. There is good agreement between the experimentally resolved Auger lifetimes and $\tau_{\text{Auger}}^{\text{BLB}}$ at high temperatures. At low temperatures though, $\tau_{\text{Auger}}^{\text{BLB}}$ deviates from the measured data. $\tau_{A1}^{(i)}$ is highly sensitive to $|F_1F_2|$, and incorrectly assuming that this parameter is temperature independent can lead to this discrepancy. A comparison between $\mathbf{k}\cdot\mathbf{p}$ calculated and $\tau_{\text{Auger}}^{\text{BLB}}$ for MCT indicates that $|F_1F_2|$ is weakly temperature dependent for that material system [11]. Because of the more complicated band structure, it is reasonable to expect that $|F_1F_2|$ may also be temperature dependent for a T2SL material system. Another explanation is that γ is finite, and a portion of the experimental Auger coefficients can be attributed to p-type Auger processes. This would reduce C_n, and the extracted low-injection Auger lifetimes would be longer in the extrinsic temperature regime. As the Auger lifetime determines the longest possible nonradiative carrier lifetime and, ultimately, the best-case photodetector dark current, a more rigorous investigation of Auger recombination in this material system is necessary to determine its fundamental limitations. However, within the uncertainty of our measurements, the BLB Auger-1 lifetime theory presented here is a reasonable predictor of low-injection Auger lifetimes in n-type InAs/InAs$_{1-x}$Sb$_x$ T2SLs.

C. Radiative recombination

The measured B coefficients are plotted as a function of temperature in Fig. 6. Unfortunately, for temperatures greater than 200 K, the radiative contribution to the total carrier lifetime is too small to be reliably determined. The measured B coefficients do follow an approximate $T^{-3/2}$ dependence up to 200 K, which is consistent with VRS theory for direct-gap semiconductors [33]. Also shown in Fig. 6 are calculated B_r coefficients determined directly from the T2SL band structure using the 14-band $\mathbf{k}\cdot\mathbf{p}$ software. Scaling these calculated values with $\phi = 15$ using Eq. (13) provides good agreement between the calculated and measured coefficients. The same scaling is shown in Fig. 4 when comparing the extracted low-injection radiative lifetimes to $\mathbf{k}\cdot\mathbf{p}$ calculated low-injection radiative lifetimes. Previous theoretical calculations predicted $\phi = 1.7$–2 for a 4-μm-thick InAs/InAs$_{1-x}$Sb$_x$ T2SL of similar composition to that investigated here [22,32]. The larger photon recycling factor extracted here is more congruent with the theory of Humphreys [48], who concludes a photon recycling factor of approximately 20 for typical refractive indices in semiconductors using first-principles calculations.

When the equilibrium electron density is taken into account during analysis of carrier lifetimes, $\tau_{\mathrm{Auger}}^{-1}$ displays a quadratic relationship with Δn as

$$\begin{aligned}\tau_{\mathrm{Auger}}^{-1} &= C_n(n_0+\Delta n)^2,\\ &= C_n n_0^2 + 2C_n n_0 \Delta n + C_n \Delta n^2, \qquad (24)\end{aligned}$$

where terms that are both independent of and linear with Δn are present. Even if the hole-dominated Auger processes are not neglected, $\tau_{\mathrm{Auger}}^{-1}$ will still contribute a term that is linear with Δn. If n_0 is ignored, this expression for $\tau_{\mathrm{Auger}}^{-1}$ is reduced to $C_n \Delta n^2$, and no linear or constant terms appear in the Auger recombination contribution to τ^{-1}. Since τ_{rad}^{-1} also displays a linear dependence with Δn, attributing the component of τ^{-1} that is linear in Δn solely to the radiative mechanism can lead to errors in the B coefficient extracted from carrier-lifetime data. For example, in semiconductor material that has large Auger rates stemming from large Auger coefficients, high doping levels, and/or high temperatures, the constant and linear terms in Eq. (24) will be significant. Erroneously attributing all linear components of τ^{-1} to the radiative mechanism will then lead to an underestimation of the radiative lifetime. For the T2SL material investigated here, this Auger contribution is, indeed, significant. The authors note that in the case where Auger recombination is an insignificant contributor to the carrier lifetime, such as is typical for InAs/In$_x$Ga$_{1-x}$Sb T2SLs, this would not be an issue.

Consideration of these effects is highlighted in Fig. 7, where a comparison of fitting results is shown when n_0 is included and excluded in the carrier-lifetime analysis. For the case where n_0 is included in the analysis, Eq. (20) is used in its entirety for fitting the measured data. In this case, both the radiative and Auger recombination contributions saturate to a constant value as Δn becomes less than n_0. The linear portion of τ^{-1} is now a combination of radiative and Auger recombination components. These lifetimes are represented by the dashed curves in Fig. 7. For the case where n_0 is excluded from the analysis, it is set to zero for the Auger and radiative lifetime components in Eq. (20). In this case, the radiative and Auger recombination contributions have a linear and squared dependence on Δn, respectively, over all injection regimes, and $\tau_{\mathrm{Auger}}^{-1}$ does not contribute a linear term to τ^{-1}. Radiative recombination is then the only mechanism that contributes to the linear portion of τ^{-1}. Note, for clarity, the SRH lifetime components are not plotted in Fig. 7. The best fits, C_n coefficients, and extracted τ_{MC} are indistinguishable for both of these cases. However, the radiative contribution and recovered B coefficients vary significantly depending on whether n_0 is included or excluded. The B coefficients when n_0 is included in the radiative and Auger lifetime terms are 2.5×10^{-12} cm^3/s and 1.0×10^{-11} cm^3/s at 200 and 100 K, respectively. When n_0 is excluded from the analysis, the B coefficients are, instead, found to be 1.0×10^{-10} cm^3/s and 8.0×10^{-11} cm^3/s at 200 and 100 K, respectively, representing an error in the extracted radiative coefficient by a factor of 40 at 200 K and 8 at 100 K. This subtlety leads to an underestimation of ϕ when comparing extracted B coefficients to calculated B_r coefficients. Using the 100-K data, ϕ would reduce from 15 to 2 if the linear component of $\tau_{\mathrm{Auger}}^{-1}$ is ignored. For the 200-K data, the B coefficient when n_0 is excluded is actually larger than the B_r value predicted by $\mathbf{k}\cdot\mathbf{p}$. This error is more significant at greater temperatures for this material system since Auger recombination has a greater overall contribution to the total lifetime. Because of the relatively large Auger coefficients measured in this material system, it is clear that the most accurate depiction of carrier recombination in InAs/InAs$_{1-x}$Sb$_x$ T2SLs must take into account the doping level and intrinsic carrier density. This result is in contrast to previous reports where the linear Auger recombination

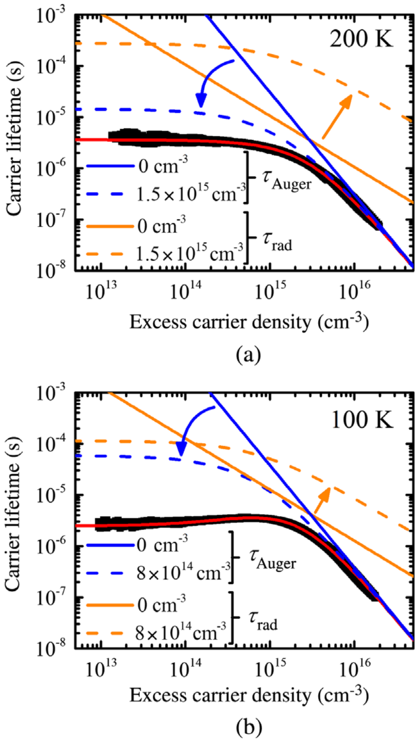

FIG. 7. Comparison of fitting results when the equilibrium electron density n_0 is included and excluded from the Auger and radiative recombination components of the total lifetime for (a) 200-K and (b) 100-K lifetime data. The red curves are the best fits to the measured data (black symbols) and are indistinguishable whether n_0 is included or excluded. The solid orange and blue curves are the radiative and Auger recombination components when n_0 is excluded from the analysis, respectively. The dashed curves are the same recombination components when n_0 is included in the analysis. The SRH lifetime components are not shown.

component to the carrier lifetime was not explicitly taken into account, and radiative recombination was found to play a more significant part in the carrier dynamics [5,22,49].

D. Calculated dark current

As stated earlier, for a diffusion-limited detector, the primary source of a dark current is J_{diff} arising from thermal generation of carriers in the undepleted absorber region. Shown in Fig. 8 are calculated diffusion dark currents using Eq. (1), the measured temperature-dependent lifetime parameters, and carrier densities for the cases where τ_{MC} is limited by SRH recombination and Auger recombination. In both cases, the doping level is set to the experimental value of $n_0 = 8 \times 10^{14}\ \mathrm{cm}^{-3}$. The radiatively limited case is not considered, since through carrier extraction, radiative recombination will be suppressed further relative to SRH and Auger recombination. Comparing the SRH- to Auger-limited T2SL cases, mitigation of the SRH defects will allow either a decrease in the dark current by approximately 2 orders of magnitude when operating at the same temperature (e.g., from $4.38 \times 10^{-7}\ \mathrm{A/cm}^2$ to $2.06 \times 10^{-9}\ \mathrm{A/cm}^2$ at 125 K) or for the same dark current, operation at 35 K greater temperature.

For comparison to current state-of-the-art detectors, also shown is the dark current for a similar band-gap MCT detector using the Rule 07 (the 07 refers to the year this result was obtained) [50]. The band gap of MCT is matched to the T2SL at 100 K (Cd composition = 0.2898) and the temperature dependence determined using $E_g(x,T) = -0.302 + 1.93x - 0.81x^2 + 0.832x^3 + 5.35 \times 10^{-4}(1-2x)T$ [51]. The T2SL underperforms compared to MCT for the SRH-limited τ_{MC} case, but it will have significantly lower dark current for the Auger-limited case. This theoretical comparison indicates that mitigation of the SRH defect states in the InAs/InAs$_{1-x}$Sb$_x$ T2SL will be beneficial, as a lower diffusion current and potentially better performance can be attained.

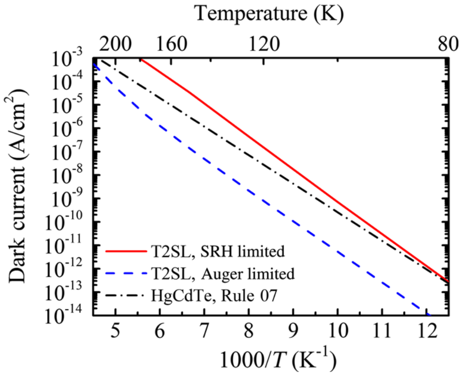

FIG. 8. Calculated dark currents using the extracted carrier-lifetime parameters and assuming the InAs/InAs$_{0.66}$Sb$_{0.34}$ superlattice is limited by Shockley-Read-Hall or Auger recombination. The doping level is set to the measured value of $8 \times 10^{14}\ \mathrm{cm}^{-3}$. Also shown is the calculated dark current for a similar band-gap Hg$_{0.7102}$Cd$_{0.2898}$Te detector determined by the Rule 07.

VI. CONCLUSION

Sensitive time-resolved microwave reflectance measurements of excess carrier decay are reported for a MWIR InAs/InAs$_{0.66}$Sb$_{0.34}$ T2SL absorber of an IR photodetector. The time-resolved decays are transformed into instantaneous carrier lifetimes as functions of the excess carrier density and analyzed using standard equations for carrier recombination. By including the known doping level of the T2SL absorber in the analysis of the lifetime data, the SRH, radiative, and Auger recombination components of the total measured lifetime are uniquely distinguished from one another, and the limiting mechanisms are identified as functions of excess carrier density at each individual temperature. This uniqueness allowed for a detailed analysis of the carrier-recombination mechanisms currently limiting a high-quality MWIR InAs/InAs$_{0.66}$Sb$_{0.34}$ T2SL.

For excess carrier densities below the T2SL doping level and for temperatures below 175 K, SRH recombination limits the minority-carrier lifetime. SRH trap saturation is also observed in the carrier-lifetime data for this temperature range. A midgap SRH defect state, either 95 meV above the T2SL valence-band edge or below the T2SL conduction-band edge, is identified from the SRH component of the minority-carrier lifetime. Auger recombination is determined to be the limiting mechanism for excess carrier densities greater than the T2SL doping level for all temperatures. Additionally, for temperatures greater than 225 K, Auger recombination limits the low-injection lifetimes due to the onset of high intrinsic electron densities. It is shown that the BLB Auger-1 lifetime theory, which is commonly used to model Auger lifetimes, is a good predictor of the temperature dependence of low-injection Auger lifetimes for the temperature range investigated. However, a more rigorous study of Auger recombination in this T2SL material system is warranted to determine the fundamental limitations more accurately. Radiative recombination is found to have no significant contribution to the measured carrier lifetime for all injection regimes and temperatures. Comparing the extracted radiative lifetimes to radiative lifetimes calculated from $\mathbf{k} \cdot \mathbf{p}$ theory suggests a photon recycling factor of 15, which is substantially larger than previously reported. It is shown that by excluding the equilibrium electron density from the analysis, the radiative lifetimes are underestimated.

Finally, complete characterization of the carrier-lifetime parameters and carrier densities allow calculation of diffusion currents for various limiting cases. These predicted diffusion currents are compared to dark currents in MCT calculated from the Rule 07 for the same band-gap energy as the T2SL investigated here. For the case of SRH-limited minority-carrier lifetimes corresponding to the measured lifetime data, the T2SL diffusion current is greater than the dark current in MCT. Since the carrier-lifetime mechanisms are uniquely distinguished in this study, T2SL diffusion currents are also predicted for the case where Auger recombination limits the minority-carrier lifetimes. In this case, the T2SL is projected to have a lower dark current than MCT by a significant margin. These results imply that significant gains can be made with InAs/InAs$_{1-x}$Sb$_x$ technology if the SRH defect states are mitigated.

ACKNOWLEDGMENTS

Sandia National Laboratories is a multiprogram laboratory managed and operated by Sandia Corporation, a wholly owned subsidiary of Lockheed Martin Corporation, for the U.S. Department of Energy's National Nuclear Security Administration under Contract No. DE-AC04-94AL85000. This project is supported by a grant from the Intelligence Community Postdoctoral Research Fellowship Program through funding from the Office of the Director of National Intelligence. All statements of fact, opinion, or analysis expressed are those of the author and do not reflect the official positions or views of the Intelligence Community or any other U.S. government agency. Nothing in the contents should be construed as asserting or implying U.S. government authentication of information or intelligence community endorsement of the authors' views. This research is partially supported through a subcontract from The University of Iowa.

[1] M. A. Kinch, Fundamental physics of infrared detector materials, J. Electron. Mater. **29**, 809 (2000).

[2] D. R. Rhiger, Performance comparison of long-wavelength infrared type-II superlattice devices with HgCdTe, J. Electron. Mater. **40**, 1815 (2011).

[3] B. V. Olson, E. A. Shaner, J. K. Kim, J. F. Klem, S. D. Hawkins, L. M. Murray, J. P. Prineas, M. E. Flatté, and T. F. Boggess, Time-resolved optical measurements of minority carrier recombination in a mid-wave infrared InAsSb alloy and InAs/InAsSb superlattice, Appl. Phys. Lett. **101**, 092109 (2012).

[4] E. H. Steenbergen, B. C. Connelly, G. D. Metcalfe, H. Shen, M. Wraback, D. Lubyshev, Y. Qiu, J. M. Fastenau, A. W. K. Liu, S. Elhamri, O. O. Cellek, and Y. -H. Zhang, Significantly improved minority carrier lifetime observed in a long-wavelength infrared III-V type-II superlattice comprised of InAs/InAsSb, Appl. Phys. Lett. **99**, 251110 (2011).

[5] L. Höglund, D. Z. Ting, A. Khoshakhlagh, A. Soibel, C. J. Hill, A. Fisher, S. Keo, and S. D. Gunapala, Influence of radiative and non-radiative recombination on the minority carrier lifetime in midwave infrared InAs/InAsSb superlattices, Appl. Phys. Lett. **103**, 221908 (2013).

[6] D. Donetsky, G. Belenky, S. Svensson, and S. Suchalkin, Minority carrier lifetime in type-2 InAs-GaSb strained-layer superlattices and bulk HgCdTe materials, Appl. Phys. Lett. **97**, 052108 (2010).

[7] B. C. Connelly, G. D. Metcalfe, H. Shen, and M. Wraback, Direct minority carrier lifetime measurements and recombination mechanisms in long-wave infrared type II superlattices using time-resolved photoluminescence, Appl. Phys. Lett. **97**, 251117 (2010).

[8] L. M. Murray, K. S. Lokovic, B. V. Olson, A. Yildirim, T. F. Boggess, and L. P. Prineas, Effects of growth rate variations on carrier lifetime and interface structure in InAs/GaSb superlattices, J. Cryst. Growth **386**, 194 (2014).

[9] D. Donetsky, S. P. Svensson, L. E. Vorobjev, and G. Belenky, Carrier lifetime measurements in short-period InAs/GaSb strained-layer superlattice structures, Appl. Phys. Lett. **95**, 212104 (2009).

[10] D. Zuo, P. Qiao, D. Wasserman, and S. L. Chuang, Direct observation of minority carrier lifetime improvement in InAs/GaSb type-II superlattice photodiodes via interfacial layer control, Appl. Phys. Lett. **102**, 141107 (2013).

[11] Y. Chang, C. H. Grein, J. Zhao, C. R. Becker, M. E. Flatté, P.-K. Liao, F. Aqariden, and S. Sivananthan, Carrier recombination lifetime characterization of molecular beam epitaxially grown HgCdTe, Appl. Phys. Lett. **93**, 192111 (2008).

[12] D. Z. -Y. Ting, C. J. Hill, A. Soibel, S. A. Keo, J. M. Mumolo, J. Nguyen, and S. D. Gunapala, A high-performance long wavelength superlattice complementary barrier infrared detector, Appl. Phys. Lett. **95**, 023508 (2009).

[13] A. M. Hoang, G. Chen, R. Chevallier, A. Haddadi, and M. Razeghi, High performance photodiodes based on InAs/InAsSb type-II superlattices for very long wavelength infrared detection, Appl. Phys. Lett. **104**, 251105 (2014).

[14] A. Khoshakhlagh, S. Myers, H. Kim, E. Plis, N. Gautam, S. J. Lee, S. K. Noh, L. R. Dawson, and S. Krishna, Long-wave InAs/GaSb superlattice detectors based on nBn and pin designs, IEEE J. Quantum Electron. **46**, 959 (2010).

[15] C. L. Canedy, E. H. Aifer, I. Vurgaftman, J. G. Tischler, J. R. Meyer, J. H. Warner, and E. M. Jackson, Antimonide type-II "*W*" photodiodes with long-wave infrared R_0A comparable to HgCdTe, J. Electron. Mater. **36**, 852 (2007).

[16] C. H. Grein, J. Garland, and M. E. Flatté, Strained and unstrained layer superlattices for infrared detection, J. Electron. Mater. **38**, 1800 (2009).

[17] C. H. Grein, P. M. Young, and H. Ehrenreich, Minority carrier lifetimes in ideal InGaSb/InAs superlattices, Appl. Phys. Lett. **61**, 2905 (1992).

[18] M. E. Flatté and C. H. Grein, Theory and modeling of type-II strained-layer superlattice detectors, Proc. SPIE Int. Soc. Opt. Eng. **7222**, 72220Q (2009).

[19] S. P. Svensson, D. Donetsky, D. Wang, H. Hier, F. J. Crowne, and G. Belenky, Growth of type II strained layer superlattice, bulk InAs and GaSb materials for minority lifetime characterization, J. Cryst. Growth **334**, 103 (2011).

[20] B. C. Connelly, G. D. Metcalfe, H. Shen, M. Wraback, C. L. Canedy, I. Vurgaftman, J. S. Melinger, C. A. Affouda, E. M. Jackson, J. A. Nolde, J. R. Meyer, and E. H. Aifer, Investigation of trap states in mid-wavelength infrared type-II superlattices using time-resolved photoluminescence, J. Electron. Mater. **42**, 3203 (2013).

[21] C. -T. Sah, R. N. Noyce, and W. Shockley, Carrier generation and recombination in P-N junctions and P-N junction characteristics, Proc. IRE **45**, 1228 (1957).

[22] B. V. Olson, E. A. Shaner, J. K. Kim, J. F. Klem, S. D. Hawkins, M. E. Flatté, and T. F. Boggess, Identification of dominant recombination mechanisms in narrow-bandgap InAs/InAsSb type-II superlattices and InAsSb alloys, Appl. Phys. Lett. **103**, 052106 (2013).

[23] J. Hwang, K. Lee, A. Teran, S. Forrest, J. D. Phillips, A. J. Martin, and J. Millunchick, Multiphoton Sub-Band-Gap Photoconductivity and Critical Transition Temperature in Type-II GaSb Quantum-Dot Intermediate-Band Solar Cells, Phys. Rev. Appl. **1**, 051003 (2014).

[24] D. -J. Jang, M. E. Flatté, C. H. Grein, J. T. Olesberg, T. C. Hasenberg, and T. F. Boggess, Temperature dependence of auger recombination in a multilayer narrow-band-gap superlattice, Phys. Rev. B **58**, 13047 (1998).

[25] D. V. Lang, Deep level transient spectroscopy: A new method to characterize traps in semiconductors, J. Appl. Phys. **45**, 3023 (1974).

[26] M. Beguwala and C. R. Crowell, Characterization of multiple deep level systems in semiconductor junctions by admittance measurements, Solid State Electron. **17**, 203 (1974).

[27] A. Chandola, R. Pino, and P. S. Dutta, Below bandgap optical absorption in tellurium-doped GaSb, Semicond. Sci. Technol. **20**, 886 (2005).

[28] M. Kunst and G. Beck, The study of charge carrier kinetics in semiconductors by microwave conductivity measurements, J. Appl. Phys. **60**, 3558 (1986).

[29] W. H. Lau, J. T. Olesberg, and M. E. Flatté, Electronic structures and electron spin decoherence in (001)-grown layered zincblende semiconductors, arXiv:cond-mat/0406201.

[30] R. K. Ahrenkiel, B. M. Keyes, and D. J. Dunlavy, Intensity dependent minority carrier lifetime in III-V semiconductors due to saturation of recombination centers, J. Appl. Phys. **70**, 225 (1991).

[31] B. Klein, N. Gautam, E. Plis, T. Shuler-Sandy, T. J. Rotter, S. Krishna, B. C. Connelly, G. D. Metcalfe, P. Shen, and M. Wraback, Carrier lifetime studies in midwave type-II InAs/GaSb strained layer superlattice, J. Vac. Sci. Technol. B **32**, 02C101 (2014).

[32] Y. Aytac, B. V. Olson, J. K. Kim, E. A. Shaner, S. D. Hawkins, J. F. Klem, M. E. Flatté, and T. F. Boggess, Effects of layer composition and alloy composition on carrier lifetimes in mid-wave infrared InAs/InAsSb superlattices, Appl. Phys. Lett. **105**, 022107 (2014).

[33] R. N. Hall, Recombination processes in semiconductors, Proc. IEEE **106**, 923 (1959).

[34] W. van Roosbroeck and W. Shockley, Photon-radiative recombination of electrons and holes in germanium, Phys. Rev. **94**, 1558 (1954).

[35] J. Blakemore, *Semiconductor Statistics* (Dover Publications, Inc., New York, 1962).

[36] A. R. Beattie, Quantum efficiency in InSb, J. Phys. Chem. Solids **23**, 1049 (1962).

[37] J. R. Lindle, J. R. Meyer, C. A. Hoffman, F. J. Bartoli, G. W. Turner, and H. K. Choi, Auger lifetime in InAs, InAsSb, and InAsSb-InAlAsSb quantum wells, Appl. Phys. Lett. **67**, 3153 (1995).

[38] M. E. Flatté, C. H. Grein, T. C. Hasenberg, S. A. Anson, D. -J. Jang, J. T. Olesberg, and T. F. Boggess, Carrier recombination rates in narrow-gap InAs/$Ga_{1-x}In_xSb$-based superlattices, Phys. Rev. B **59**, 5745 (1999).

[39] C. H. Grein, M. E. Flatté, J. T. Olesberg, S. A. Anson, L. Zhang, and T. F. Boggess, Auger recombination in narrow-gap semiconductor superlattices incorporating antimony, J. Appl. Phys. **92**, 7311 (2002).

[40] S. Anikeev, D. Donetsky, G. Belenky, S. Luryi, C. A. Wang, J. M. Borrego, and G. Nichols, Measurement of the Auger recombination rate in p-type 0.54 eV GaInAsSb by time-resolved photoluminescence, Appl. Phys. Lett. **83**, 3317 (2003).

[41] C. H. Grein, P. M. Young, M. E. Flatté, and H. Ehrenreich, Long wavelength InAs/InGaSb infrared detectors: Optimization of carrier lifetimes, J. Appl. Phys. **78**, 7143 (1995).

[42] C. M. Ciesla, B. N. Murdin, T. J. Phillips, A. M. White, A. R. Beattie, C. J. G. M. Landerak, C. T. Elliot, C. R. Pidgeon, and S. Sivananthan, Auger recombination dynamics of $Hg_{0.795}Cd_{0.205}Te$ in the high excitation regime, Appl. Phys. Lett. **71**, 491 (1997).

[43] Z. M. Fang, K. Y. Ma, D. H. Ma, D. H. Jaw, R. M. Cohen, and G. B. Stringfellow, Photoluminescence of InSb, InAs, and InAsSb grown by organometallic vapor phase epitaxy, J. Appl. Phys. **67**, 7034 (1990).

[44] C. H. Grein, M. E. Flatté, A. J. Evans, A. D. Hood, W. E. Tennant, and V. Nathan, Design of phosphorus-containing MWIR type-II superlattices for infrared photon detectors, IEEE J. Sel. Top. Quantum Electron. **19**, 1 (2013).

[45] E. R. Youngdale, J. R. Meyer, C. A. Hoffman, F. J. Bartoli, C. H. Grein, P. M. Young, H. Ehrenreich, R. H. Miles, and D. H. Chow, Auger lifetime enhancement in InAs-$Ga_{1-x}In_xSb$ superlattices, Appl. Phys. Lett. **64**, 3160 (1994).

[46] A. R. Beattie and P. T. Landsberg, Auger effect in semiconductors, Proc. R. Soc. A **249**, 16 (1959).

[47] O. Madelung, *Semiconductors: Data Handbook*, 3rd ed. (Springer-Verlag, Berlin, 2004).

[48] R. G. Humphreys, Radiative lifetime in semiconductors for infrared detection, Infrared Phys. **23**, 171 (1983); Radiative lifetime in semiconductors for infrared detection **26**, 337 (1986).

[49] L. Höglund, D. Z. Ting, A. Soibel, A. Fisher, A. Khoshakhlagh, C. J. Hill, S. Keo, and S. D. Gunapala, Minority carrier lifetime in mid-wavelength infrared InAs/InAsSb superlattices: Photon recycling and the role of radiative and Shockley-Read-Hall recombination mechanisms, Appl. Phys. Lett. **105**, 193510 (2014).

[50] W. Tennant, Interpreting mid-wave infrared MWIR HgCdTe photodetectors, Prog. Quantum Electron. **36**, 273 (2012).

[51] G. L. Hansen, J. L. Schmit, and T. N. Casselman, Energy gap versus alloy composition and temperature in $Hg_{1-x}Cd_xTe$, J. Appl. Phys. **53**, 7099 (1982).